


Evolution of conditionally averaged second-order structure functions in a transitional boundary layer

H. Yao **Department of Aeronautics, Imperial College London, London SW7 2AZ, United Kingdom*F. Alves-Portela †*School of Engineering Sciences, University of Southampton, Southampton SO17 1BJ, United Kingdom*G. Papadakis ‡*Department of Aeronautics, Imperial College London, London SW7 2AZ, United Kingdom*

(Received 14 April 2020; accepted 27 August 2020; published 25 September 2020)

We consider the bypass transition in a flat-plate boundary layer subject to free-stream turbulence and compute the evolution of the second-order structure function of the streamwise velocity, $\langle du^2 \rangle(\vec{x}, \vec{r})$, from the laminar to the fully turbulent region using DNS. In order to separate the contributions from laminar and turbulent events at the two points used to define $du(\vec{x}, \vec{r})$, we apply conditional sampling based on the local instantaneous intermittency, τ (1 for turbulent and 0 for laminar events). Using $\tau(\vec{x}, t)$, we define two-point intermittencies, $\gamma^{(TT)}$, $\gamma^{(LL)}$, and $\gamma^{(TL)}$, which physically represent the probabilities that both points are in turbulent patches, both are in laminar patches, or one is in a turbulent and the other in a laminar patch, respectively. Similarly, we also define the conditionally averaged structure functions, $\langle du^2 \rangle^{(TT)}$, $\langle du^2 \rangle^{(LL)}$, and $\langle du^2 \rangle^{(TL)}$, and decompose $\langle du^2 \rangle(\vec{x}, \vec{r})$ in terms of these conditional averages. The derived expressions generalize existing decompositions of single-point statistics to two-point statistics. It is found that in the transition region, laminar streaky structures maintain their geometrical characteristics in the physical and scale space well inside the transition region, even after the initial breakdown to form turbulent spots. Analysis of the $\langle du^2 \rangle^{(TT)}$ fields reveals that the outer mode is the dominant secondary instability mechanism. Further analysis reveals how turbulent spots penetrate the boundary layer and approach the wall. The peaks of $\langle du^2 \rangle^{(TT)}$ in scale space appear in larger streamwise separations as the transition progresses and this is explained by the strong growth of turbulent spots in this direction. On the other hand, the spanwise separation where the peak occurs remains relatively constant and is determined by the initial inception process. We also analyze the evolution of the two-point intermittency field, $\gamma^{(TT)}$, at different locations. In particular, we study the growth of the volume enclosed within an isosurface of $\gamma^{(TT)}$ and note that it increases in both directions, with growth in the streamwise direction being especially large. The evolution of these conditional two-point statistics sheds light on the transition process from a different perspective and complements existing analyses using single-point statistics.

DOI: [10.1103/PhysRevFluids.5.093902](https://doi.org/10.1103/PhysRevFluids.5.093902)

*hy3717@ic.ac.uk

†f.alves-portela@soton.ac.uk

‡g.papadakis@ic.ac.uk

I. INTRODUCTION

Boundary layer transition affects the performance of many engineering devices. For example, in aeronautical applications, it increases friction drag, thereby increasing fuel costs and the emission of harmful pollutants to the environment. When the disturbances are relatively strong, e.g., a high turbulent intensity in the free stream (larger than about 0.51%), roughness, acoustic waves, etc., the transition process bypasses the natural route of Tollmien-Schlichting waves; this is called bypass transition [1].

In the present paper, we consider bypass transition due to free-stream turbulence, which has been studied extensively through experiments [2–5] and numerical simulations [6–9]. The transition starts with the penetration of low-frequency free-stream modes inside the boundary layer, while the high-frequency ones remain outside due to shear sheltering [10,11]. Forward (high-speed) and backward (low-speed) streaks are then formed, which were called Klebanoff modes by Kendall [2,12]. The mechanism of streak formation can be explained by rapid distortion theory [13]. The strong streamwise amplification is due to the liftup effect (see [14] for a review and refer also to Landahl [15] for a description of how streaks are generated through a vortex tilting process). Mathematically, in the context of bypass transition, it is more appropriate to explain the growth as the resonant solution of the Squire equation for the wall normal vorticity when forced by the continuous Orr-Sommerfeld modes that have a sinusoidal shape and reside in the free stream (see [8] for more details and a perspective review [16] that summarizes the different points of view for streak formation and growth).

The streaky structures evolve as they propagate downstream; the low-speed ones lift up to the edge of the boundary layer, interacting with high-frequency modes in the free stream. Secondary instability occurs due to this interaction, causing turbulent spots, which eventually lead to breakdown to turbulence [6]. This process is explored in [17], which describes the streak breakdown from a three-dimensional perspective (sinuous secondary instability). More recently, Vaughan and Zaki [18] used Floquet theory to analyze idealized unsteady streaks that appear inside the boundary layer when forced by monochromatic (i.e., single-frequency) modes. They found that the Kelvin-Helmholtz-type secondary instability is of two types: ‘outer’ and ‘inner.’ In a follow-up work, Hack and Zaki [19] successfully predict the localized secondary instability of particular streaks under broadband free-stream forcing.

Intermittent turbulent spots appear after the breakdown of the laminar streaky structures. The first description of turbulent spots appeared in the experimental work of Emmons [20]. Following from this early work, artificially generated spots were studied by experimentalists in visualization studies [21–23]. Anthony *et al.* [24] explored turbulent spots in bypass transition, showing that spots due to free-stream turbulence differ from conventional spots (spots in Emmons’ experiment [20]). More recently, a numerical study of turbulent spots in bypass transition was done by Wu *et al.* [25]. Hairpin packets were found before streaks, and then the packets directly led to the formation of turbulent spots. Using conditional sampling, Nolan and Zaki [26] studied the growth of turbulent spots in terms of the propagation rate and size under different external pressure gradients. Further research by Marxen and Zaki [27] examined the intermittent turbulence characteristics in the bypass transition region. Both conditional and ensemble averaging were used to study the intermittent turbulent spots. They found that in the core region of the spots, first- and second-order statistics are similar to those of a fully turbulent flow.

Most of the aforementioned work has focused on one-point statistics, i.e., the distribution of mean velocities, normal and shear stresses, etc. As mentioned by Eckhardt [28], one of the challenging questions in transition is the emergence of the turbulent cascade. This provides the motivation to employ two-point statistics in order to investigate the transition process. Previous two-point analyses have employed the velocity correlation function [3,4,9,29]. For example, Matsubara and Alfredsson [4] investigated the streamwise velocity correlation function and found that the spanwise length scale, which corresponds to the minimum of the correlation, does not vary much in the streamwise direction. The detailed behavior is dependent on the grid used to generate the free-stream turbulence;

in some cases it increases, and in others it decreases. On the other hand, when scaled with the displacement thickness of the boundary layer, δ^* , it approaches a constant value, approximately $3\delta^*$ for all cases. They found also that the streaks have a streamwise length scale, which increases along the downstream direction. In the DNS of transition due to high-intensity free-stream turbulence of [9], the evolution of the velocity correlation function was also found to be case dependent. For the case of a small turbulence length scale at the inlet, which is more similar to the one examined in this paper, the spacing of streaks (in physical units) was found to slowly increase along the downstream distance. On the other hand, when normalized with δ^* , it decays slowly; values close to $2\delta^*$ have been reported. Theoretical analysis using optimal perturbation theory applied to the Navier-Stokes equations linearized around the Blasius velocity profile [30,31] show that the maximum amplification is found for a spanwise wave number, β^* , that scales with δ^* as $\beta^*\delta^* = 0.77$. This corresponds to a minimum in the correlation function located at $4.08\delta^*$, thus it is expected to grow as $\sim x^{1/2}$ when expressed in physical units. In the experiments and DNS, the growth is generally found to be slower, which may be due to the nonlinear effects induced by transition. The experiments in [3] also indicate slower growth.

In this paper, instead of using two-point velocity correlation functions, we employ the second-order structure function for the fluctuation of the streamwise velocity, u . This is a two-point statistical quantity, defined as $\langle du^2 \rangle = \langle (u^+ - u^-)^2 \rangle$, where the superscript plus and minus signs indicate two points in space. Their coordinates are defined using the midpoint $\vec{X} = (X, Y, Z)$ and the separation vector $\vec{r} = (r_1, r_2, r_3)$, i.e., $\vec{x}^\pm = \vec{X} \pm \vec{r}/2$. Similarly to the velocity correlation, $\langle du^2 \rangle$ is also a six-dimensional quantity, $\langle du^2 \rangle(X, Y, Z, r_1, r_2, r_3)$. We prefer, however, to work with the second-order structure function, as opposed to the two-point correlation, for the following reasons:

- i. There is no loss of information, because there is a direct relationship between these two-point statistical quantities, $\langle du^2 \rangle = \langle (u^+ - u^-)^2 \rangle = \langle (u^+)^2 \rangle + \langle (u^-)^2 \rangle - 2\langle u^+ u^- \rangle$; the last term is the velocity correlation function.
- ii. It has a more clear physical meaning, because $\langle du^2 \rangle + \langle dv^2 \rangle + \langle dw^2 \rangle$ can be regarded as the scale energy in physical space, i.e., it quantifies the energy contained within an eddy of size (length scale) $|\vec{r}|$, which is centered at point $\vec{X} = (X, Y, Z)$; refer to [32] for more details on this interpretation and the caveats for small $|\vec{r}|$. In the above sum, $\langle du^2 \rangle$ has the highest contribution, so this term is a good approximation of the scale energy. Since the structure function is formulated in physical space, it is applicable to spatially varying flows.
- iii. Its transport equation is the generalized Karman-Howarth equation [33,34], which has been increasingly used as a statistical tool for the analysis of interscale energy transfer in inhomogeneous and anisotropic flows, for example, channel flow [35], flow around a square prism [36], and flow in the wake of a fractal grid [37].

Additionally, since we are studying a transitional flow, it is of interest to analyze the effect of intermittency on the statistics of $\langle du^2 \rangle$ via conditional sampling. Although this approach has long been applied to single-point statistics [38], we could not find a similar analysis for two-point statistics in the literature. We therefore derive the relevant equations and study the conditionally averaged fields. As shown, many interesting physical features of transition can be elucidated from the analysis of these fields.

The paper is organized as follows. In the next section, Sec. II, we briefly describe the numerical method and show a comparison with reference results from the literature (computational or experimental) for validation purposes. We then proceed in Sec. III to derive the decomposition of the conditionally averaged $\langle du^2 \rangle$. In Sec. IV we analyze $\langle du^2 \rangle$ in the laminar and fully turbulent regions, and in Sec. V the evolution of the conditionally averaged fields in the transitional region. In Sec. VI we study the two-point intermittency field $\gamma^{(TT)}$, and finally, we conclude in Sec. VII.

II. NUMERICAL METHOD AND ONE-POINT STATISTICS (VALIDATION T3A CASE)

The DNS simulation was performed using our in-house finite-volume solver, Pantarhei, a finite-volume solver for Navier-Stokes equations that employs the fractional step method to enforce the

continuity equation and update the pressure at every time step. For more details and applications of the solver to various transitional and fully turbulent flows refer to [36] and [39–41].

The spatial coordinates are normalized by the Blasius similarity variable, $L_0 = \sqrt{\nu X_0/U_\infty}$, where X_0 is the distance of the domain inlet from the leading edge of the plate. The computational domain size is $3000 \times 200 \times 150$ in the streamwise (X), wall-normal (Y), and spanwise (Z) directions, respectively. The numbers of cells in each direction are $2049 \times 192 \times 169$. The mesh is uniform in the streamwise and spanwise directions, while in the wall-normal direction the cells grow with expansion ratio 1.06 until $Y = 20L_0$; farther away from the wall the mesh is uniform. The resulting spacings in wall units (indicated by a superscript plus sign) are $\Delta x_{\max}^+ \sim 11.78$, $\Delta y_{\max}^{+(w)} \sim 0.24$, and $\Delta z_{\max}^+ \sim 7.14$. The subscript “max” denotes maximum values (found in the fully turbulent region), while $\Delta y_{\max}^{+(w)}$ is evaluated at the centroid of the first cell close to the wall. The inlet Reynolds number is $\text{Re}_{L_0} = 160$.

We let the flow develop for a sufficiently long time to reach statistical steady state and then collect statistics for three flow-through times. The time step is set to $0.2T_0$ (where $T_0 = L_0/U_\infty$), which results in a maximum CFL number of around 0.35. Two-point statistics are calculated from 350 samples with time and spanwise averaging. The time separation between two samples is $20T_0$, i.e., we sample every 100 time steps. Convergence is reported in Fig. 18 in the Appendix, where $\langle du^2 \rangle$ is plotted vs the number of samples at a fixed streamwise position (located in the turbulent region) and wall-normal distance, for small and large streamwise separations r_1 (and $r_3 = 0$). It can be seen that after about 200 samples, the average has reached a converged value. Similar results are found at other streamwise positions, wall-normal locations, and separations.

The free-stream turbulent intensity, Tu , is set to 3.4% to match the transition onset location; this is close to the 3.5% value of Jacob and Durbin [6]. The Von Karman spectrum

$$E(k) = \text{Tu}^2 \frac{1.196(kL_{11})^4}{[0.558 + (kL_{11})^2]^{17/6}} L_{11}, \quad \text{Tu} = 3.4\%, \quad L_{11} = 5L_0, \quad (1)$$

is assumed for the turbulent fluctuations in the free stream. The length scale is set to $L_{11} = 5L_0$, which is approximately equal to the boundary layer thickness at the inlet.

For generation of the inlet conditions that satisfy the aforementioned spectrum, we follow a process similar to previous DNS simulations [7]. To check the implementation of the inlet conditions, in Fig. 1(a) we compare the decay rate of the free-stream turbulence intensity with the results of Jacob and Durbin [6]; we note that the two sets of results match well. The skin friction coefficient, C_f , vs the momentum thickness, Re_θ , also matches well with the T3A experiments [42], as shown in Fig. 1(b). There is a small deviation for $250 < \text{Re}_\theta < 350$, where the current result is slightly lower than the experimental data. In Jacob’s work, the C_f is slightly overestimated (refer to Fig. 4 in Ref. [6]).

In Fig. 1(c) we compare the mean streamwise velocity (in wall units) with the T3A experiment [42]. In the late transition and fully turbulent region the matching is good, however, the mean velocity in the transition region is more difficult to match. This is due to differences in the free-stream conditions that are very difficult to reproduce exactly. Figure 1(d) displays the profile of $\text{rms}(u)/\text{rms}(u)_{\max}$ vs the Blasius variable, η . The circles are calculated using the raw data from the T3A database [42]. The profile matches well (up to $\eta \approx 4$) with the normalized shape of $\eta F''$, where F'' is the Blasius function. The latter formula was originally used by Taylor [43] and Klebanoff [2] for experimental data fitting. The streamwise velocity fluctuation profile clearly indicates the presence of the so-called Klebanoff modes.

It is instructive at this point to visualize some instantaneous velocity fields. In the left panels in Fig. 2, we use the instantaneous wall-normal fluctuation velocity, v , to visualize turbulent structures (spots) at $Y/L_0 = 5$. A large, fully formed structure can be seen at the right in the top-left panel. Note the rapid change of the sign of v over the structure. A smaller structure, just forming, can be discerned in the area $(X - X_0)/L_0 \approx 1050\text{--}1100$ and $Z/L_0 \approx 25$. We track the growth of this

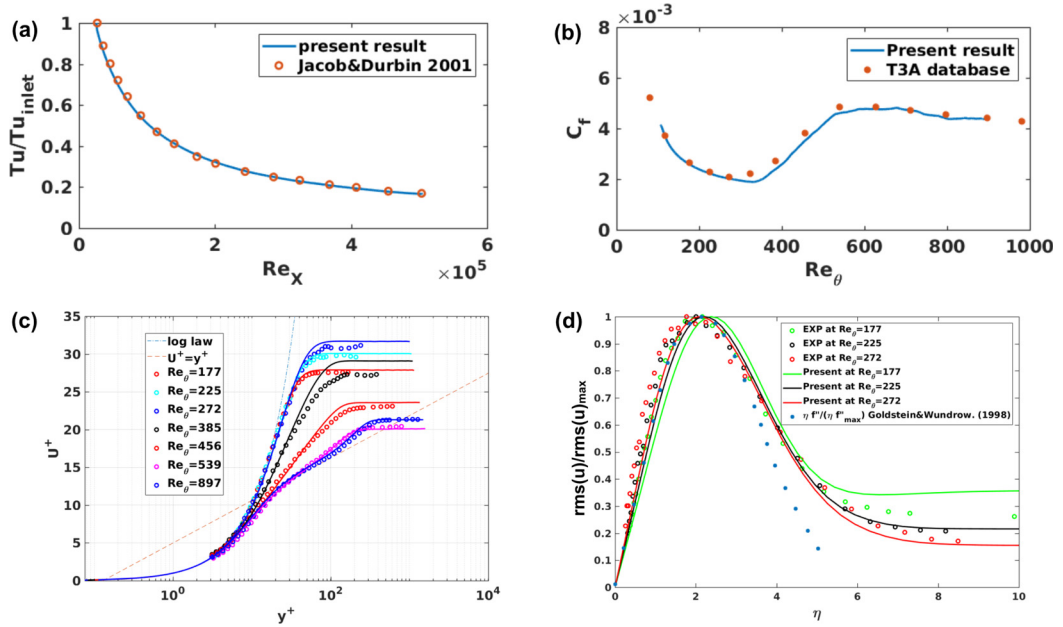


FIG. 1. (a) Free-stream turbulent intensity Tu vs Re_x ; (b) skin friction coefficient C_f vs Re_θ ; (c) mean streamwise velocity U^+ vs y^+ ; (d) $rms(u)/rms(u)_{max}$ vs the Blasius variable, η .

turbulent structure at four instants in time (left panels, from top to bottom). The growth of the structure in the streamwise and spanwise directions is evident.

In the right panels in Fig. 2, we show the contours of the instantaneous streamwise velocity fluctuations through the center of the spot, at the same instants. The horizontal domain visualized

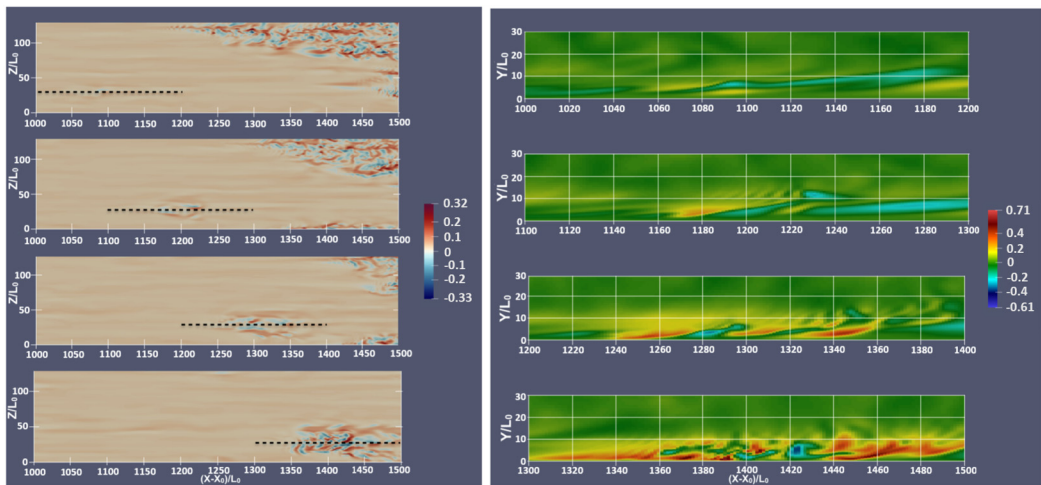


FIG. 2. Flow snapshots tracking a spot from its incipient formation (top row) to its fully developed form (bottom row); wall-normal velocity fluctuations at $Y = 5L_0$ (left panels); streamwise velocity fluctuations in the plane at $Z = 25L_0$ (indicated as horizontal dashed lines in the left panels) that pass through the center of the spot (right panels). Note the translation of the domain visualized in the streamwise direction in the right panels. The time interval between each snapshot is $190L_0/U_\infty$.

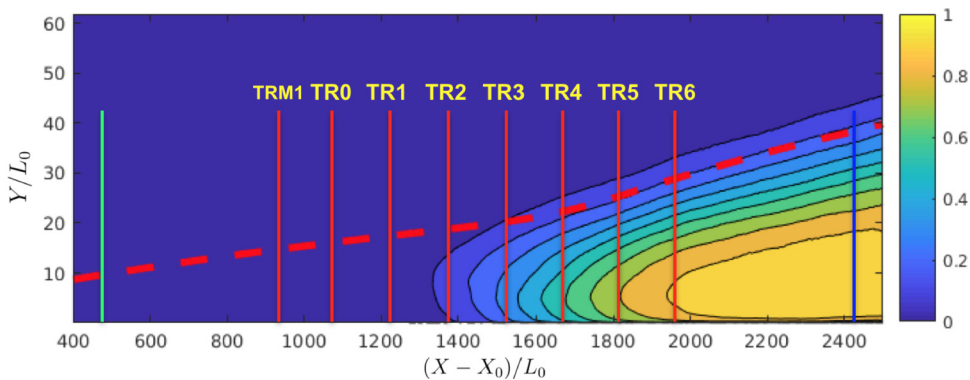


FIG. 3. Contour plot of the intermittency field γ . The dashed red line represents the boundary layer thickness. The solid green, red, and blue vertical lines represent the streamwise locations where the second-order structure functions are calculated. The green line is in the laminar region ($(X - X_0)/L_0 = 540$) and the blue line in the turbulent region ($(X - X_0)/L_0 = 2415$). The eight red lines, $TRM1$ and $TR0 - TR6$, are in the transition region and their coordinates are 940, 1065, 1215, 1365, 1515, 1665, 1815, and 1965, respectively.

in the right panels is shifted in the streamwise direction in order to account for the translating motion of the structure; the domain shown corresponds to the horizontal dashed lines in the left panels. In the top-right panel, we see the lifting-up of the low-speed streak (negative fluctuating velocities). The velocity field at this instant in time is smooth, but in the panel below the footprints of secondary instability start to appear at $Y \sim 12L_0$, $(X - X_0)/L_0 \sim 1180-1220$. The turbulent motion moves closer to the wall and fills the boundary layer below $10L_0$; a fully formed spot has been formed, as can be seen in the bottom row (left and right panels). The observed growth of spots cannot be captured with single-point statistics, but as shown later, two-point statistics, especially ones conditioned on turbulent events, is a very effective statistical tool for this purpose.

III. DERIVATION OF CONDITIONALLY AVERAGED TWO-POINT STATISTICS

A. Binary indicator function

We define an instantaneous binary indicator function, $\tau(X, Y, Z, t)$, that takes the value 1 if the flow is turbulent and 0 if it is laminar. Similarly to the work by Marxen and Zaki [27], this indicator function is based on the standard deviation of $D = |v| + |w|$, where v and w are the wall-normal and spanwise velocities, respectively (using the standard deviation to detect the turbulent patches is consistent with the snapshots shown in Fig. 2). We also use Otsu's method [44] to find an optimal threshold to identify the turbulent and nonturbulent regions.

The time and spanwise average of the τ field

$$\gamma(X, Y) = \frac{1}{\Delta T L_z} \int_0^{\Delta T} \int_0^{L_z} \tau(X, Y, Z, t) dz dt \quad (2)$$

is known as the intermittency, γ . A contour plot is shown in Fig. 3; it is very similar to Fig. 5 in [27]. By arguing that turbulent spots are born with equal probability, Narasimha [45] proposed a 'universal' distribution for intermittency, which matches well with the present result of $\gamma_{\max}(X) = \max(\gamma(X, Y))$, as shown in Fig. 4.

The binary indicator function and the intermittency field allow us to define conditional averaged statistics, as explained in the next subsection.

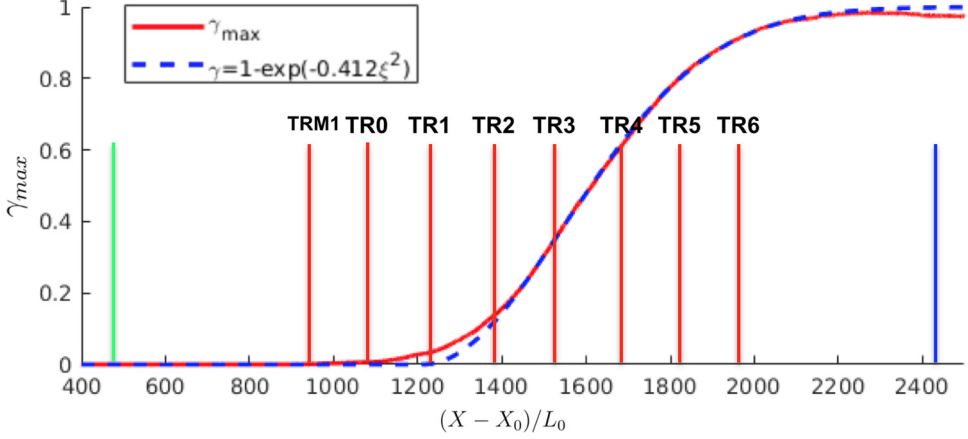


FIG. 4. Variation of γ_{\max} (solid line) in the streamwise direction and comparison with the formula of Narashima (dashed line), where $\xi = (X - X_s)/(X_{\gamma=0.75} - X_{\gamma=0.25})$, and X_s is the location where the transition starts, taken to be $(X_s - X_0)/L_0 = 1100$.

B. Derivation of the conditional two-point structure function

We start by summarizing the existing expressions for single-point statistics. We use capital symbols, for example, U_i and Φ , to denote instantaneous quantities and lowercase symbols, u_i and ϕ , to denote fluctuations around a time- and spanwise-averaged variable, $\langle U_i \rangle$ or $\langle \Phi \rangle$.

A conventionally averaged quantity, $\langle \Phi \rangle$, can be decomposed into conditionally averaged quantities using the intermittency γ as

$$\langle \Phi \rangle = \gamma \langle \Phi \rangle^{(T)} + (1 - \gamma) \langle \Phi \rangle^{(L)}, \quad (3)$$

where the superscripts (T) and (L) indicate averages conditioned on turbulent and laminar events, respectively. The conditionally averaged variables are defined as

$$\langle \Phi \rangle^{(T)} = \frac{1}{\Delta T L_z \gamma} \int_0^{\Delta T} \int_0^{L_z} \tau \Phi dz dt, \quad \langle \Phi \rangle^{(L)} = \frac{1}{\Delta T L_z (1 - \gamma)} \int_0^{\Delta T} \int_0^{L_z} (1 - \tau) \Phi dz dt. \quad (4)$$

Using the Reynolds decomposition $\phi = \Phi - \langle \Phi \rangle$, the variance of fluctuations can be written as

$$\langle \phi^2 \rangle = \langle \Phi^2 \rangle - \langle \Phi \rangle^2, \quad (5)$$

and similarly for the conditional variances,

$$\langle \phi^2 \rangle^{(T)} = \langle \Phi^2 \rangle^{(T)} - (\langle \Phi \rangle^{(T)})^2, \quad \langle \phi^2 \rangle^{(L)} = \langle \Phi^2 \rangle^{(L)} - (\langle \Phi \rangle^{(L)})^2. \quad (6)$$

The variance can also be written in terms of conditional-averaged quantities as [38]

$$\langle \phi^2 \rangle = \gamma \langle \phi^2 \rangle^{(T)} + (1 - \gamma) \langle \phi^2 \rangle^{(L)} + \gamma(1 - \gamma) (\langle \Phi \rangle^{(T)} - \langle \Phi \rangle^{(L)})^2. \quad (7)$$

We can employ the same decomposition for the time- and spanwise-averaged Reynolds stresses. The latter can be written in terms of conditional-averaged quantities as [27,38]

$$\langle u_i u_j \rangle = \gamma \langle u_i u_j \rangle^{(T)} + (1 - \gamma) \langle u_i u_j \rangle^{(L)} + \gamma(1 - \gamma) (\langle U_i \rangle^{(T)} - \langle U_i \rangle^{(L)}) (\langle U_j \rangle^{(T)} - \langle U_j \rangle^{(L)}). \quad (8)$$

We can extend this decomposition to two-point statistics; the two points are indicated by the plus- and minus-sign superscripts. The conditional averaging now includes three different states, which are defined as follows:

$$\text{States} = \begin{cases} \text{turbulent-turbulent (TT)}, & \tau^+ = 1, \quad \tau^- = 1; \\ \text{turbulent-laminar (TL)} & \tau^+ = 1, \quad \tau^- = 0 \quad \text{or} \quad \tau^+ = 0, \quad \tau^- = 1; \\ \text{laminar-laminar (LL)} & \tau^+ = 0, \quad \tau^- = 0. \end{cases} \quad (9)$$

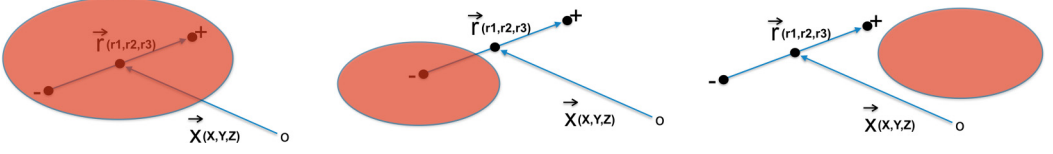


FIG. 5. Sketches of the three states. Red ovals represent turbulent spots. Both points within a turbulent spot (state TT ; left); one point inside a turbulent spot, the other in the laminar region (state TL ; middle); both points in the laminar region (state LL ; right).

A schematic for each state is shown in Fig. 5.

Using the identity

$$\tau^+ \tau^- + (\tau^+(1 - \tau^-) + (1 - \tau^+) \tau^-) + (1 - \tau^+)(1 - \tau^-) = 1, \quad (10)$$

the instantaneous velocity difference $dU = U^+ - U^-$ can be written as

$$dU = \tau^+ \tau^- dU + (\tau^+(1 - \tau^-) + (1 - \tau^+) \tau^-) dU + (1 - \tau^+)(1 - \tau^-) dU. \quad (11)$$

Taking the time and spanwise average of the above equation, we get the decomposition

$$\langle dU \rangle = \gamma^{(TT)} \langle dU \rangle^{(TT)} + \gamma^{(TL)} \langle dU \rangle^{(TL)} + \gamma^{(LL)} \langle dU \rangle^{(LL)}, \quad (12)$$

where

$$\begin{aligned} \langle dU \rangle^{(TT)} &= \frac{1}{\Delta T L_z \gamma^{(TT)}} \int_0^{\Delta T} \int_0^{L_z} \tau^+ \tau^- (U^+ - U^-) dz dt, \\ \langle dU \rangle^{(TL)} &= \frac{1}{\Delta T L_z \gamma^{(TL)}} \int_0^{\Delta T} \int_0^{L_z} (\tau^+(1 - \tau^-) + (1 - \tau^+) \tau^-) (U^+ - U^-) dz dt, \\ \langle dU \rangle^{(LL)} &= \frac{1}{\Delta T L_z \gamma^{(LL)}} \int_0^{\Delta T} \int_0^{L_z} (1 - \tau^+)(1 - \tau^-) (U^+ - U^-) dz dt \end{aligned} \quad (13)$$

are the conditional averages and

$$\begin{aligned} \gamma^{(TT)} &= \frac{1}{\Delta T L_z} \int_0^{\Delta T} \int_0^{L_z} \tau^+ \tau^- dz dt, \\ \gamma^{(TL)} &= \frac{1}{\Delta T L_z} \int_0^{\Delta T} \int_0^{L_z} (\tau^+(1 - \tau^-) + (1 - \tau^+) \tau^-) dz dt, \\ \gamma^{(LL)} &= \frac{1}{\Delta T L_z} \int_0^{\Delta T} \int_0^{L_z} (1 - \tau^+)(1 - \tau^-) dz dt \end{aligned} \quad (14)$$

are the two-point intermittencies; the latter generalize Eq. (2). Due to the identity, (10), their sum is

$$\gamma^{(TT)} + \gamma^{(TL)} + \gamma^{(LL)} = 1. \quad (15)$$

Definition (14) indicates that $\gamma^{(TT)}$, $\gamma^{(TL)}$, $\gamma^{(LL)}$ can be physically interpreted as probabilities. For example, $\gamma^{(TT)}$ is the probability that both points \vec{x}^\pm are located within turbulent patches; similar interpretations can be given to $\gamma^{(TL)}$ and $\gamma^{(LL)}$. The sum of the probabilities is equal to 1 [Eq. (15)], and (12) is a weighted sum that involves the probabilities of the three states and the corresponding conditional averages.

Similarly to the single-point case, the variance and conditional variance for the fluctuations difference can be written as

$$\begin{aligned} \langle du^2 \rangle &= \langle dU^2 \rangle - \langle dU \rangle^2, & \langle du^2 \rangle^{(TT)} &= \langle dU^2 \rangle^{(TT)} - (\langle dU \rangle^{(TT)})^2, \\ \langle du^2 \rangle^{(TL)} &= \langle dU^2 \rangle^{(TL)} - (\langle dU \rangle^{(TL)})^2, & \langle du^2 \rangle^{(LL)} &= \langle dU^2 \rangle^{(LL)} - (\langle dU \rangle^{(LL)})^2. \end{aligned} \quad (16)$$

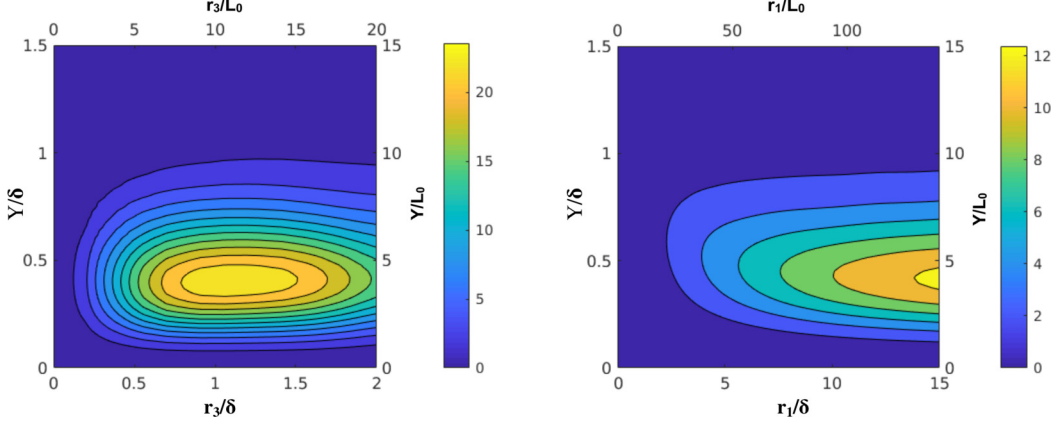


FIG. 6. $\langle du^2 \rangle$ on the (r_3, Y) (left) and (r_1, Y) (right) planes in the laminar region. Note that the left and bottom axes are normalized by the local boundary layer thickness (δ), while the top and right axes are normalized by the inlet Blasius similarity variable, L_0 .

Using Eqs. (12) and (16) and after some algebra, we obtain the decomposition of $\langle du^2 \rangle$,

$$\langle du^2 \rangle = \gamma^{(TT)} \langle du^2 \rangle^{(TT)} + \gamma^{(TL)} \langle du^2 \rangle^{(TL)} + \gamma^{(LL)} \langle du^2 \rangle^{(LL)} + \Psi(\langle dU \rangle^{(TT)}, \langle dU \rangle^{(TL)}, \langle dU \rangle^{(LL)}), \quad (17)$$

where

$$\Psi(\langle dU \rangle^{(TT)}, \langle dU \rangle^{(TL)}, \langle dU \rangle^{(LL)}) = \gamma^{(TT)} (\langle dU \rangle^{(TT)})^2 + \gamma^{(TL)} (\langle dU \rangle^{(TL)})^2 + \gamma^{(LL)} (\langle dU \rangle^{(LL)})^2 - (\gamma^{(TT)} \langle dU \rangle^{(TT)} + \gamma^{(TL)} \langle dU \rangle^{(TL)} + \gamma^{(LL)} \langle dU \rangle^{(LL)})^2. \quad (18)$$

The above equation generalizes the existing decomposition of single-point statistics, Eq. (7), to two-point ones. We checked its validity by performing numerical experiments with synthetic data.

IV. TWO-POINT STRUCTURE FUNCTION IN THE LAMINAR AND TURBULENT REGIONS

In this section, contour plots of the time- and spanwise-averaged streamwise structure functions on the (r_3, Y) and (r_1, Y) planes at the streamwise locations X_i , shown as solid vertical lines in Fig. 3, are presented. For each plane, we consider that the other separations are 0. For example, for the (r_1, Y) plane we plot $\langle du^2 \rangle(r_1, Y; X_i, r_2 = 0, r_3 = 0)$, while for the (r_3, Y) plane we plot $\langle du^2 \rangle(r_3, Y; X_i, r_1 = 0, r_2 = 0)$. For all plots, the values are normalized by the square of the local friction velocity, $u_\tau^2(X_i)$.

The conventionally averaged $\langle du^2 \rangle$ is first plotted in the laminar and turbulent regions. This is followed by similar plots in the transitional region, and finally, we present maps of the conditionally averaged quantities.

A. Streaky laminar region

The structure function in the streaky laminar region, corresponding to the green line in Fig. 3, is shown in Fig. 6. Note that the separations in the spanwise and streamwise directions as well as the wall-normal distance are normalized by two scales: one local (boundary layer thickness, δ) and one global (inlet Blasius variable, L_0).

A clear peak can be observed in the $\langle du^2 \rangle$ on the (r_3, Y) plane as shown in the left panel in Fig. 6. The peak corresponds to $r_3 \approx 1.1\delta$ (or $r_3 \approx 3\delta^*$, or $r_3 \approx 10\text{-}11L_0$ in global units). As mentioned in Sec. I, in the homogeneous direction, $\langle du^2 \rangle = 2(\langle u^2 \rangle - \langle u^+ u^- \rangle)$, and due to the negative sign

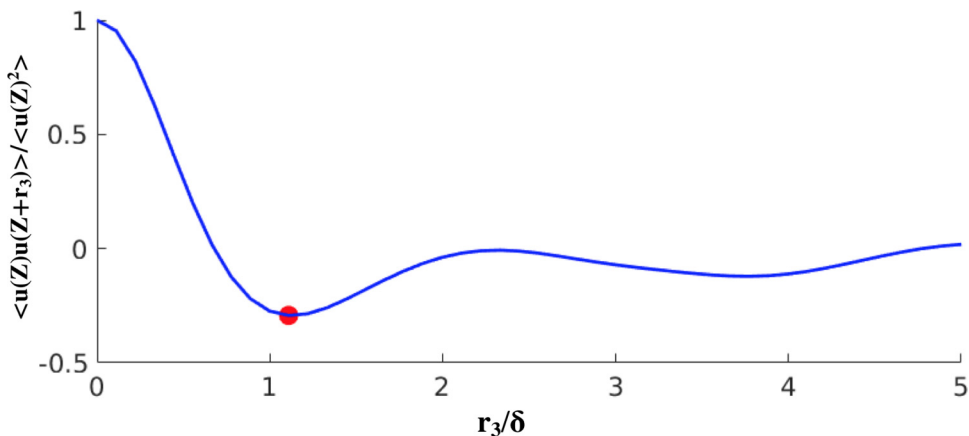


FIG. 7. Second-order streamwise velocity correlation function with respect to the spanwise separation at the wall-normal distance $Y_0 \sim 4L_0$.

before the correlation term, the minimum of the $\langle u^+ u^- \rangle$ corresponds to a maximum of the structure function. This distance is the average spacing between the laminar high- and low-speed streaks. The value $r_3 \approx 1.18$ matches the location of the first minimum point of the streamwise two-point velocity correlation function (red circle in Fig. 7). When normalized with the displacement thickness, the value of $\approx 3\delta^*$ is within the region reported in experimental and numerical theoretical studies [4,9] but smaller than $4.08\delta^*$, the value predicted by the optimal perturbation theory of [30,31]. This may be related to the fact that the peak in the optimal perturbation (Fig. 2 in Ref. [30]) is not very sharp, and the exact value selected is determined by the imposed length scale and the intensity of the free-stream turbulence at the inlet.

The scale energy peak in the wall-normal direction is located at $Y \approx 0.4\delta$ (or $Y \approx 4L_0$). This indicates the presence of Klebanoff modes, where the largest turbulent intensity of streamwise fluctuation is located around the middle of the laminar boundary layer [4,30]. This is also consistent with the one-point statistics shown in Fig. 1(d), i.e., peak at $\eta \approx 2.2$ (with thickness $\eta \approx 5$).

The right panel in Fig. 6 shows the structure function on the (r_1, Y) plane. The largest values are also located at $Y \approx 0.4\delta$ as expected, but $\langle du^2 \rangle$ increases continuously with the streamwise separation r_1 , even until the maximum value considered, $r_1 = 15\delta$. We have examined also larger separations (plots not shown) and found that $\langle du^2 \rangle$ continues to increase, but at a slower rate. We expect that at very large r_1 , the velocity fluctuations at the two points \vec{x}^\pm will become uncorrelated and $\langle du^2 \rangle$ will tend to $\langle (u^+)^2 \rangle + \langle (u^-)^2 \rangle$. If the flow were homogeneous in the streamwise direction, then $\langle du^2 \rangle$ would tend to a constant value, equal to $2\langle u^2 \rangle$; this is nicely shown in Fig. 2 in Ref. [46]. In our case, however, the flow has strong spatial inhomogeneity and $\langle du^2 \rangle$ continues to increase for large r_1 , but at a reduced rate.

B. Fully turbulent region

The structure function in the fully turbulent region corresponding to the blue line in Fig. 3 is shown in Fig. 8. Again we normalize the separations and wall-normal distances using local wall units (bottom axes) as well as the global reference quantity L_0 (top axes). On the (r_3, Y) plane (left panel), a peak is found at $r_3^+ \approx 70$ and $Y^+ \approx 16$. This corresponds to the spanwise distance of the near-wall streaks and the energy peak region is located in the buffer layer. The results are very similar to the structure function calculated for channel flow [35,47]. In terms of global units, the maximum is located at $r_3 \approx 7-8L_0$, while in the laminar region it is at $r_3 \approx 10-11L_0$. It is also closer to the wall, because the mean velocity profile has become steeper (as can be seen from the C_f coefficient) and the production takes place closer to the wall. From the (r_1, Y) plane (right panel), we

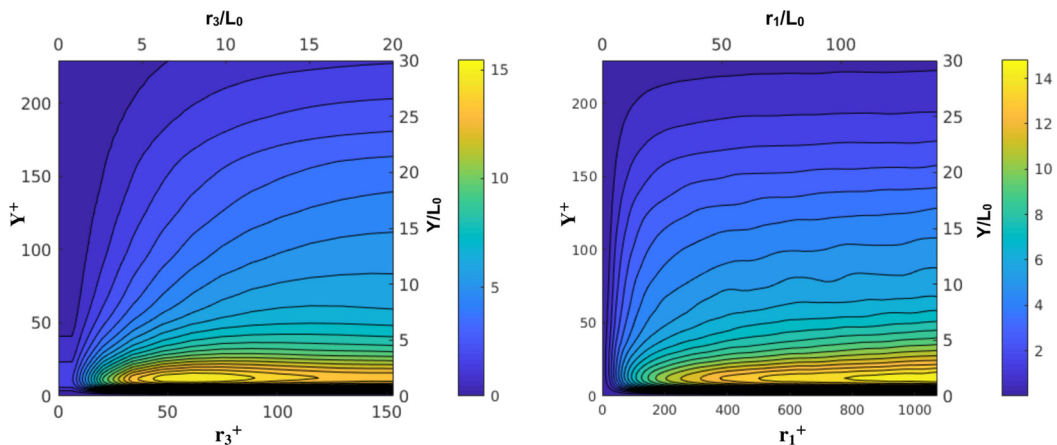


FIG. 8. $\langle du^2 \rangle$ on the (r_3, Y) (left) and (r_1, Y) (right) planes in the fully turbulent region. The left and bottom axes are in local wall units, while the top and right axes are in global units of L_0 .

can see that the structure function grows over much larger separations in the streamwise direction compared to the spanwise one; this is indicative of very long streaky structures. Again the largest values in the wall-normal direction for different separations are located within the buffer layer, at $Y^+ \approx 16$, as expected.

V. TWO-POINT STRUCTURE FUNCTION MAPS IN THE TRANSITIONAL REGION

In this section, we plot maps of the standard and conditionally averaged structure functions in the transition region on the (r_3, Y) and (r_1, Y) planes, at the locations of the red lines shown in Fig. 3.

A. Evolution of the standard structure function on the $(r_3/r_1, Y)$ plane

In Fig. 9, we see the morphing of the structure functions on the (r_3, Y) plane from the laminarlike to the turbulentlike shape; compare with the left panels in Figs. 6 and 8, respectively. In the

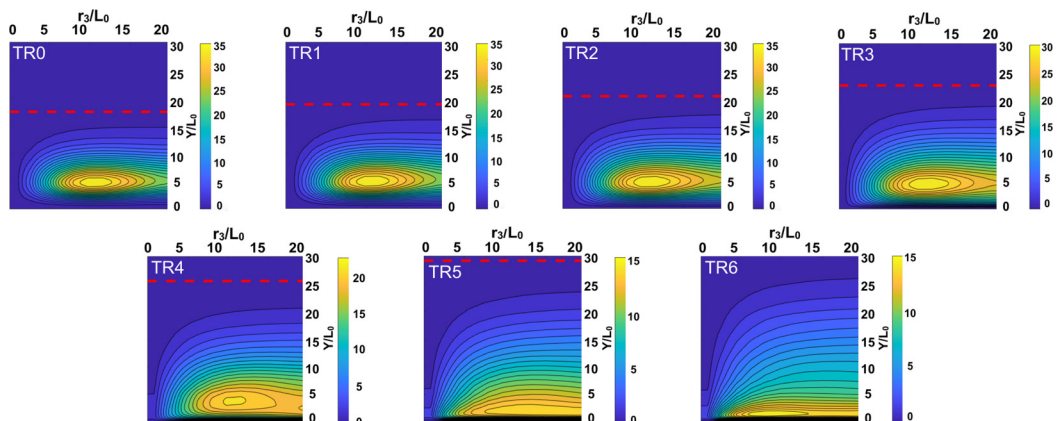


FIG. 9. Evolution of $\langle du^2 \rangle$ on the (r_3, Y) plane along the streamwise direction. The locations, denoted TR0-TR6, are defined in Fig. 3. In this and all subsequent figures, the dashed red line represents the local boundary layer thickness.

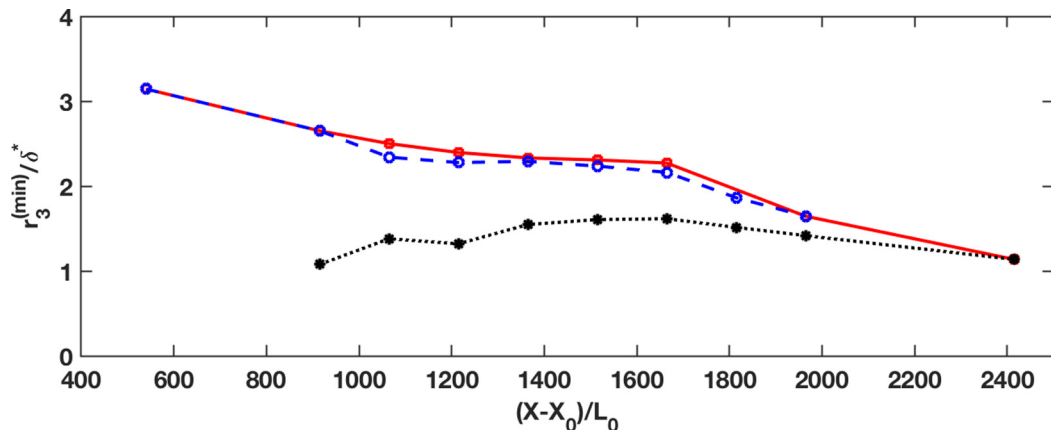


FIG. 10. Variation of the $r_3^{(\min)}/\delta^*$ along the streamwise direction. The solid red line refers to the maps of $\langle du^2 \rangle$ in Fig. 9, while the dashed blue and dotted black lines refer to the maps of $\gamma^{(LL)}\langle du^2 \rangle^{(LL)}$ in Fig. 12 and $\gamma^{(TT)}\langle du^2 \rangle^{(TT)}$ in Fig. 14, respectively. Circles mark the streamwise locations of Fig. 3.

streamwise locations $TR0$ - $TR3$, the characteristics of the laminar streaks are largely retained, i.e., the peak appears at $Y \approx 5L_0$ (slightly farther from the wall compared to the distance of $4L_0$ in the fully laminar regime) and $r_3 \approx 10L_0$. At later stages, however, starting from $TR4$, and more evidently in $TR5$ and $TR6$, the shape changes significantly and the peak location approaches closer to the wall, $Y \approx 1.6L_0$. The spanwise location of the peak, however, is maintained up to $TR5$, and only in $TR6$ it is reduced to the turbulent value of $7-8L_0$.

In Fig. 10 we plot the location of the peak normalized with the displacement thickness, $r_3^{(\min)}/\delta^*$ (solid red line). The values are between 2 and 3 until the late stage of transition [location $TR4$; $(X - X_0)/L_0 \approx 1700$] and match the numerical results in [9] [Fig. 12, in which $r_3^{(\min)}$ tends to $2\delta^*$] and the experimental results in [4] [Fig. 8, in which $r_3^{(\min)}$ tends to $3\delta^*$]. Differences might be due to the different inlet conditions of the free-stream turbulence. After $TR4$ the spacing decreases, approaching the value for the fully turbulent region.

Similarly to the results on the (r_3, y) plane, the structure function $\langle du^2 \rangle$ on the (r_1, Y) plane, shown in Fig. 11, morphs from a laminarlike to a turbulentlike shape. The peak of the scale energy moves from $Y \approx 5L_0$ down to $Y \approx 1.6L_0$. It appears that at $TR3$, there is an extended peak

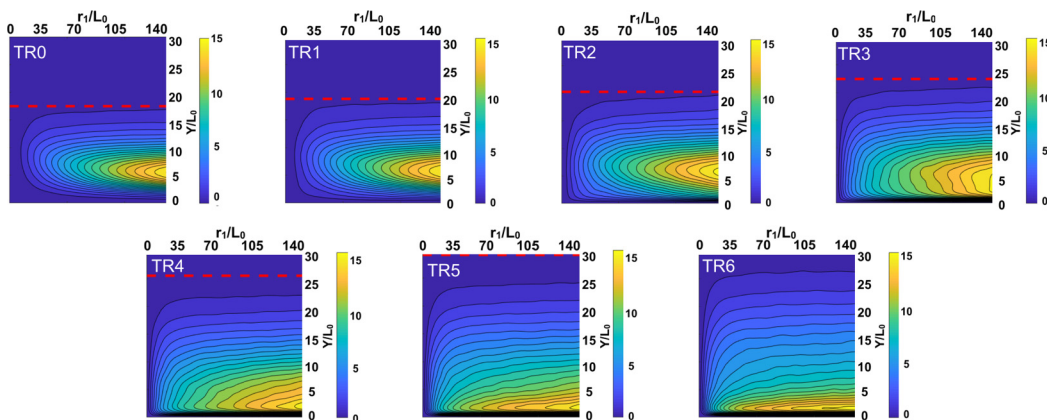


FIG. 11. Evolution of $\langle du^2 \rangle$ on the (r_1, Y) plane in the transitional region.

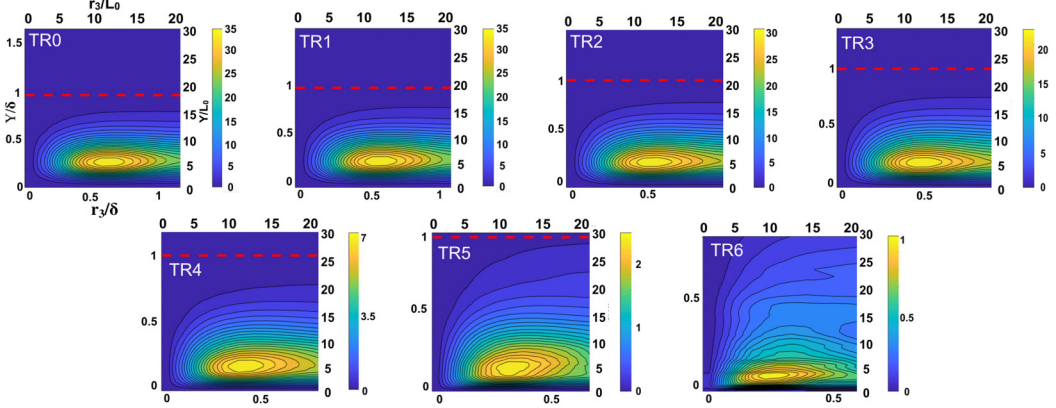


FIG. 12. Evolution of $\gamma^{(LL)}\langle du^2 \rangle^{(LL)}$ on the (r_3, Y) plane.

region from $Y \approx 1-5L_0$. This is the streamwise location where the peaks amalgamate, and farther downstream the bottom peak starts to dominate.

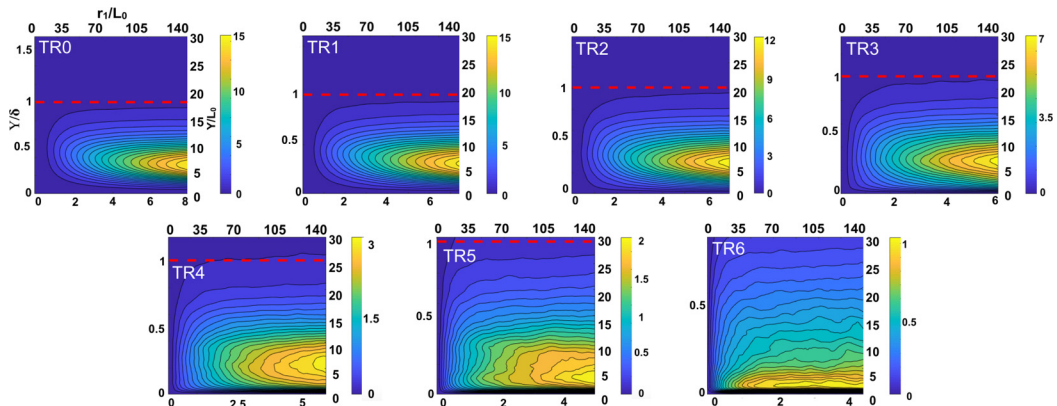
The structure functions presented above evolve smoothly between the two limiting shapes presented in Sec. IV. However, standard time and spanwise averaging conceals important information. The next subsections present the evolution of conditionally averaged structure functions. As shown, the latter provide richer information about the transition, especially when the conditioning is based on turbulent events.

B. Evolution of the structure function on the $(r_3/r_1, Y)$ plane conditioned on laminar events

The evolution of $\gamma^{(LL)}\langle du^2 \rangle^{(LL)}$ is shown in Fig. 12. Note that we chose to plot $\gamma^{(LL)}\langle du^2 \rangle^{(LL)}$, instead of $\langle du^2 \rangle^{(LL)}$, because the former appears in the decomposition, (17). It is evident that the laminar streaks persist throughout the transition, retaining the same spanwise length scale and peak energy location, i.e., peak at $r_3 \approx 11L_0$ and $Y \approx 5L_0$. It is also interesting to observe that the peak energy stays at $Y \approx 5L_0$, even though the boundary layer is growing (the dashed red lines represent the thickness of the boundary layer). Compare, for example, the bottom row in Fig. 12 with that in Fig. 9; the differences at locations $TR4$ and $TR5$ are striking. In the last plot for $TR6$, the laminar characteristics become less clear and the peak of $\gamma^{(LL)}\langle du^2 \rangle^{(LL)}$ decreases to $r_3 \approx 8L_0$. The plot is also less smooth compared to the other plots, because in the late stages of transition streaks start to merge with the turbulent boundary layer, thereby reducing the number of samples available for averaging conditioned on laminar events.

The variation of $r_3^{(\min)}/\delta^*$ along X is also shown in Fig. 10, by the dashed blue line. It is similar to the red line, i.e., the values slowly decrease to $2.3\delta^*$, remain nearly constant, and then decrease more rapidly (as expected due to the rapid growth of δ^*).

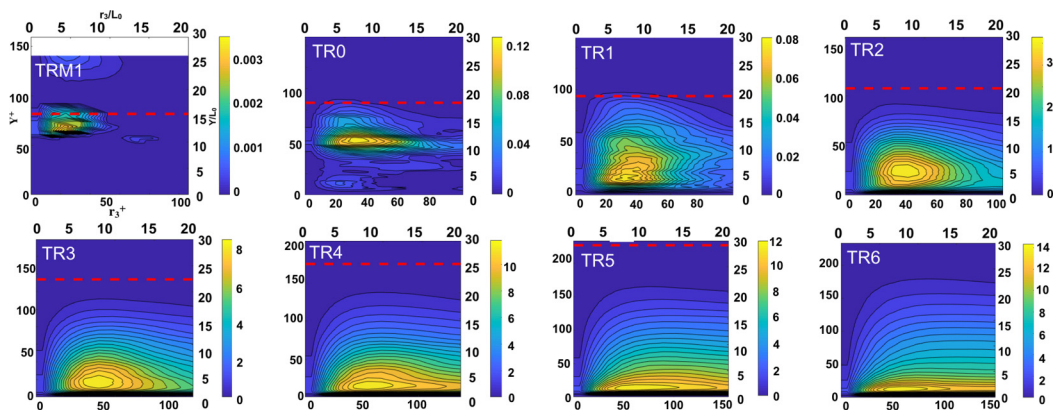
Similar conclusions can be made for the (r_1, Y) maps, shown in Fig. 13. The laminar streaky structures retain their characteristics deep into the transition region. Indeed, compared with Fig. 11, we note strong similarities for locations $TR0-TR2$ as expected, but for $TR3$ and $TR4$ we observe significant differences; in Fig. 13 the shape of the latter two is much closer to the laminar shape. For $TR5$ and $TR6$ the shape again becomes similar to that shown in Fig. 11. Even though we condition on laminar events, the underlying average flow has been modified and its footprint is reflected in the $\gamma^{(LL)}\langle du^2 \rangle^{(LL)}$ maps and the peak appears closer to the wall. As before, the plot for $TR6$ is not very smooth because of the reduced number of valid samples.

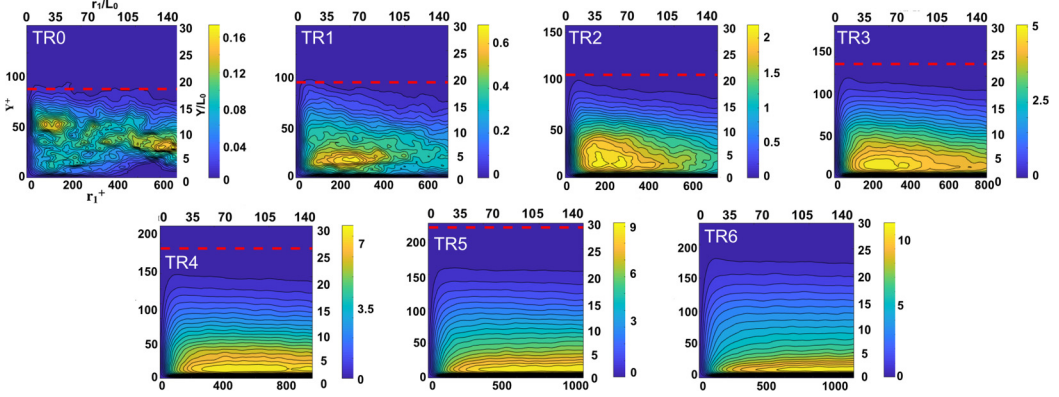

FIG. 13. Evolution of $\gamma^{(LL)}\langle du^2 \rangle^{(LL)}$ on the (r_1, Y) plane.

C. Evolution of the structure function on the $(r_3/r_1, Y)$ plane conditioned on turbulent events

The maps conditioned on turbulent events are shown in Fig. 14. It is very interesting to note that, at the earliest stage of transition at location $TR0$, turbulent motions exist near the middle of the boundary layer, with a spanwise length scale $\approx 7.5L_0$. These motions can be detected only when we apply conditional averaging; indeed they are absent when we apply standard time and spanwise averaging as evidenced in Fig. 9. This demonstrates that the proposed conditional sampling can reveal features that would not have been possible to bring to the fore otherwise.

The presence of turbulent motions in the middle of the boundary layer at the very early stages of transition is consistent with the outer type of secondary instability mentioned in [18]. In order to shed more light into this feature, we have considered one more location, $TRM1$, located upstream of $TR0$, as shown in Fig. 3. At this location, we can clearly see that the turbulent activity starts near the edge of the boundary layer, at $Y \approx 12L_0$, entirely consistent with the instantaneous pattern shown in Fig. 2 (second row from the top, on the right). The spanwise length scale at this earlier location is $5L_0$, exactly equal to the length scale L_{11} that we impose on the energy spectrum at the inlet, Eq. (1). Note also that the turbulent motions outside the boundary layer, i.e., in the free stream, are also captured and have the imposed length scale of $L_{11} = 5L_0$.


FIG. 14. Evolution of $\gamma^{(TT)}\langle du^2 \rangle^{(TT)}$ on the (r_3, Y) plane; their corresponding locations are $TRM1$ and $TR0$ - $TR6$, shown in Fig. 3.


 FIG. 15. Evolution of $\gamma^{(TT)}\langle du^2 \rangle^{(TT)}$ on the (r_1, Y) plane.

The succession of maps also demonstrates how the turbulent motions that were initiated at the top of the boundary layer penetrate deep inside it and approach the wall quite early, even at *TR1* and more clearly in *TR2*. These near-wall coherent structures (turbulent spots) become more visible in the late stages of the transition *TR4-TR6*.

It is very instructive to compare Figs. 12 and 14, which show $\gamma^{(LL)}\langle du^2 \rangle^{(LL)}$ and $\gamma^{(TT)}\langle du^2 \rangle^{(TT)}$, respectively, on the (r_3, Y) plane. When conditioning on laminar events, the peak is located at separation $r_3 \approx 10$ at all positions *TR0-TR6*; as already mentioned, this is very close to the peak observed in the laminar state (see left panel in Fig. 6). When conditioning on turbulent events, however, the location moves to $r_3 \approx 7-8$ at all streamwise positions, very close to the peak for the fully turbulent state (see left panel in Fig. 8). The two states, therefore, coexist during the whole transition process, and most importantly both retain their structural and geometric features, which are determined at their inception. For the laminar state, the inception of Klebanoff modes is determined by the receptivity process between the free-stream turbulence and the laminar boundary layer; for the turbulent state, by the secondary instability. Note that it is only through conditional averaging that we can elucidate these important characteristics.

We note that in the experiments in [29] with and without boundary layer suction, the spanwise scale of the streaky structures was found to be the same, despite a twofold reduction in the thickness of the boundary layer during suction. This led the authors to conclude that the length scale was determined by the receptivity process, which was the same for both cases. This is in accordance with our findings. The present results are also consistent with those of Marxen and Zaki [27]. Using conditional averaging, they demonstrated the similarity of the first-order statistics between spots and fully turbulent flow at the late stages of transition (not in the baby spots).

The variation of $r_3^{(\min)}/\delta^*$ is also shown in Fig. 10 by the dotted black line. The first point, at *TRM1*, and the last one, in the fully turbulent region, show a difference of 5%, but the two peaks are located at very different wall-normal distances. This figure also shows very clearly the coexistence of two length scales that correspond to the two different states of the flow.

Figure 15 shows similar behavior on the (r_1, Y) plane, i.e., turbulent motions start near the top half of the boundary layer and then penetrate towards the wall; again, this is consistent with the outer-type secondary instability [18]. However, the (r_1, Y) maps are distinctly different compared with the (r_3, Y) ones. In the latter, as we have just shown, the r_3 separation corresponding to the maximum value of $\gamma^{(TT)}\langle du^2 \rangle^{(TT)}$ was nearly constant throughout the transition process. From the (r_1, Y) maps, however, it is evident that the separation r_1 corresponding to the maximum increases significantly, from $r_1 \approx 30L_0$ to $r_1 > 140L_0$. The peak area also becomes long and flat. There is a very clear physical explanation for this change of the length scale in the r_1 direction; it is due to the

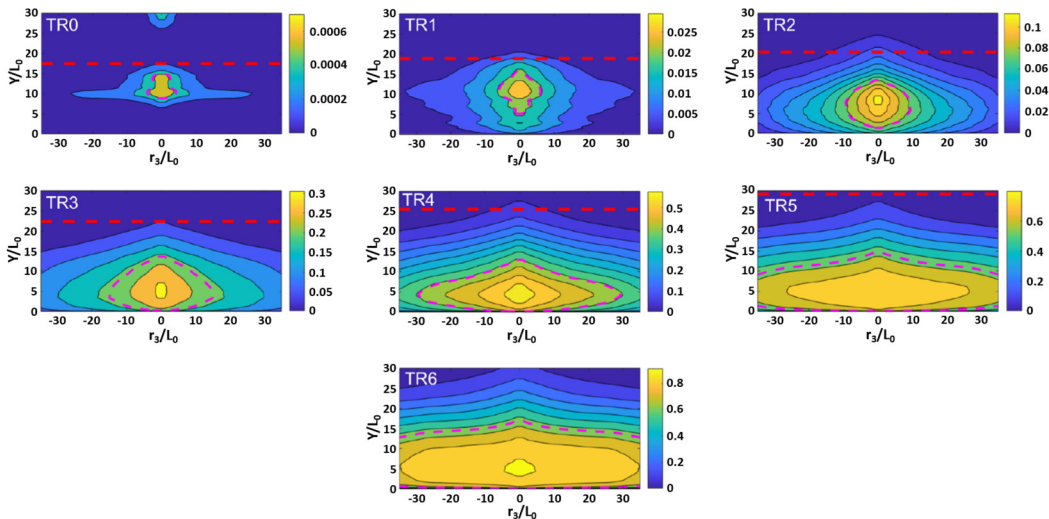


FIG. 16. Evolution of $\gamma^{(TT)}$ on the (r_3, Y) plane; pink isolines are defined as $\gamma^{(TT)} = 0.7\gamma_{\max}^{(TT)}$.

longitudinal growth of the structures within the turbulent spots. We explore this growth in the next section, by investigating the three-dimensional structure of the $\gamma^{(TT)}$ fields.

VI. TWO-POINT INTERMITTENCY FIELD $\gamma^{(TT)}$

The intermittency $\gamma(X, Y)$ shown in Fig. 3 is a single-point, two-dimensional quantity and is not suitable for analysis of the spot growth. On the other hand, the two-point intermittency field, $\gamma^{(TT)}$, contains a lot more information and, as we show below, is a more appropriate quantity to use; for this reason, in this section, we focus on $\gamma^{(TT)}$.

As mentioned in Sec. III, $\gamma^{(TT)}(X, Y; r_1, r_2, r_3)$ has a clear physical interpretation as the probability that both points $\vec{x}^\pm = \vec{X} \pm \vec{r}/2$ are located in turbulent patches or spots (but not necessarily the same spots). This probability is of course equal to the percentage of time that both points spend inside turbulent spots (averaged in the spanwise direction). It is clear that setting the separation distance to 0, i.e., $r_1 = r_2 = r_3 = 0$, results in $\gamma^{(TT)}(X, Y; 0, 0, 0) = \gamma(X, Y)$, i.e., the intermittency shown in Fig. 3.

Let us now fix the physical location (X, Y) and consider an isosurface of constant $\gamma^{(TT)}(r_1, r_2, r_3)$ and the volume of fluid enclosed by this surface. Based on the aforementioned interpretation, the fluid contained within this volume has a probability greater than or equal to the value of the isosurface of being within one (or more) turbulent region. This does not mean that this isosurface indicates the shape of a turbulent spot. The proper way to identify the spot shape is to follow the tracking method described in [27]. Nevertheless, we would expect the volume enclosed within an isosurface of constant value to grow as the transition process develops, in a similar way as a spot grows.

In Fig. 16 we plot $\gamma^{(TT)}$ on the (r_3, Y) plane at different streamwise locations, i.e., we assume $r_1 = 0$, $r_2 = 0$. The distribution of $\gamma^{(TT)}$ for $r_3 = 0$ in each map corresponds to the intermittency shown in Fig. 3. In essence, then, this figure shows the spanwise extent of the turbulent region at each streamwise location. The dashed pink lines indicate the isosurface $\gamma^{(TT)} = 0.7\gamma_{\max}^{(TT)}$, where $\gamma_{\max}^{(TT)}$ is the maximum value for the particular X location. Note that the plots are symmetric with respect to $r_3 = 0$. Indeed, $\gamma^{(TT)}$ does not depend on the sign of r_3 ; a negative value will simply swap the points \vec{x}^\pm without changing $\gamma^{(TT)}$. The same is valid for all separations, i.e., $\gamma^{(TT)}(X, Y; r_1, r_2, r_3) = \gamma^{(TT)}(X, Y; -r_1, -r_2, -r_3)$.

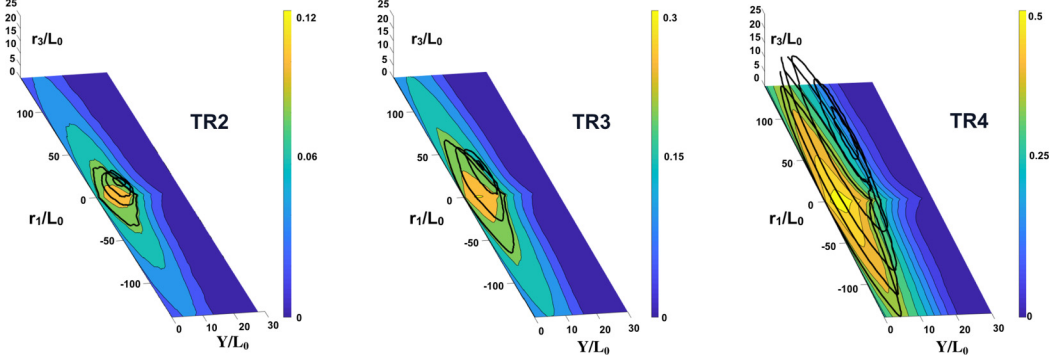


FIG. 17. Three-dimensional plots of $\gamma^{(TT)}$ at streamwise locations $TR2$, $TR3$, and $TR4$ (from left to right). Black isolines denote $\gamma^{(TT)} = 0.7\gamma_{\max}^{(TT)}$ ($r_3 = 0$).

The plots in Fig. 16 are consistent with the scenario in the previous section. At $TR0$ the peak of the $\gamma^{(TT)}$ is located at $Y \approx 10-12$ and occupies a narrow region. It then moves in the wall-normal direction and expands horizontally in the r_3 direction. It is evident that the spot forms in the top half of the boundary layer and then gradually fills the lower part. This corresponds to the top-down mechanism due to outer-type instability [26]. This top-to-bottom process can also be seen in the plots on the (r_1, Y) plane, which is similar to the results on the (r_3, Y) plane (not shown here).

In Fig. 17 three-dimensional plots of $\gamma^{(TT)}$ in the (r_1, r_3, Y) domain are shown for three streamwise locations: $TR2$, $TR3$, and $TR4$. Each plot was obtained by considering different values of r_3 and computing $\gamma^{(TT)}(r_1, Y; r_3)$ and stacking the results. For $TR2$ we considered the values $r_3 = 0, 3, 5, 6$; for $TR3$ and $TR4$, $r_3 = 0, 5, 10, 12$ and $r_3 = 0, 5, 10, 12, 13, 15, 20, 21$, respectively. The black isolines are defined as $\gamma^{(TT)} = 0.7\gamma_{\max}^{(TT)}$, where $\gamma_{\max}^{(TT)}$ is evaluated at $r_3 = 0$ (the black line on the bottom contour); the values of $\gamma_{\max}^{(TT)}$ are 0.084, 0.21, and 0.35 for $TR2$, $TR3$, and $TR4$, respectively. In these plots, a large volume can be observed with a long streamwise length and much shorter spanwise extent. The size of the volume increases along with the streamwise direction, as expected. This feature explains the growth of the r_1 separation shown in Fig. 15.

VII. CONCLUSIONS

We use the second-order structure function of the streamwise velocity as a statistical tool to explore bypass transition due to free-stream turbulence in a flat-plate boundary layer. In order to account for the intermittent formation of turbulent spots during the transition process, we derive a new decomposition of the time- and spanwise-averaged structure function in terms of conditionally averaged quantities. The conditioning process is based on the instantaneous state of the flow at the two points that are used to define the structure function. Three states are defined: (a) both points are in turbulent patches (TT state), (b) both are in the laminar region (LL state), and (c) one is in the laminar region and the other in a turbulent patch (LT state). The derived expressions generalize existing expressions for one-point statistics to two-point statistics. This analysis sheds light on the process of bypass transition from a new perspective.

The conditional structure functions are calculated along the streamwise direction, at eight locations, from the laminar region to the fully turbulent. The results conditioned on the laminar state indicate that the laminar streaks maintain their physical features even after mixing with the intermittent turbulent spots. Results conditioned on the turbulent state show that the initial turbulent motion starts near the boundary layer edge, consistent with the so-called outer secondary instability. Again, the spanwise length scale of the turbulent spots is retained throughout the transition, but the streamwise increases significantly. Only through the use of conditional statistics can these features be clearly elucidated. The two-point intermittency $\gamma^{(TT)}$ was also examined. We noted the growth

in the volume of fluid enclosed by isosurfaces of this quantity along both directions. The growth was observed mostly along the r_1 separation, indicative of the large increase in the length of the turbulent spots.

We close this section with some thoughts on future perspectives. Recall that $\langle du^2 \rangle + \langle dv^2 \rangle + \langle dw^2 \rangle$ (where $\langle du^2 \rangle$ makes the largest contribution) represents the energy contained within an eddy of size $|\vec{r}|$ which is centered at point $\vec{X} = (X, Y, Z)$. Its evolution is governed by the Karman-Howarth equation, which is valid for general inhomogeneous flows, so it is applicable to the present case. Using the database generated, we can compute the rate of energy transfer between structures of different length scales and use this information to draw the energy flow paths that determine the growth of turbulent spots. Furthermore, it is well known that spots merge to form larger spots. This implies an inverse energy transfer process, i.e., energy flowing from small to large scales, in contrast to the standard view of forward cascade (energy from large to small scales). Is there a competition between extracting energy from the mean flow (forward cascade) and from the inverse cascade process? What is the relative contribution of these two mechanisms? Future work in this direction will help to answer such questions.

ACKNOWLEDGMENTS

The authors would like to thank the U.K. Turbulence Consortium for providing computational time at the U.K. supercomputing facility ARCHER via EPSRC Grant No. EP/R029326/1. The first author would also like to acknowledge the financial support from the Department of Aeronautics and the Imperial College-CSC scholarship.

APPENDIX: CONVERGENCE OF $\langle du^2 \rangle$ WITH THE NUMBER OF SAMPLES

Figure 18 shows two examples of convergence of $\langle du^2 \rangle$ with an increasing number of samples. The location considered is in the fully turbulent region, $(X - X_0)/L_0 = 2415$, and the wall-normal

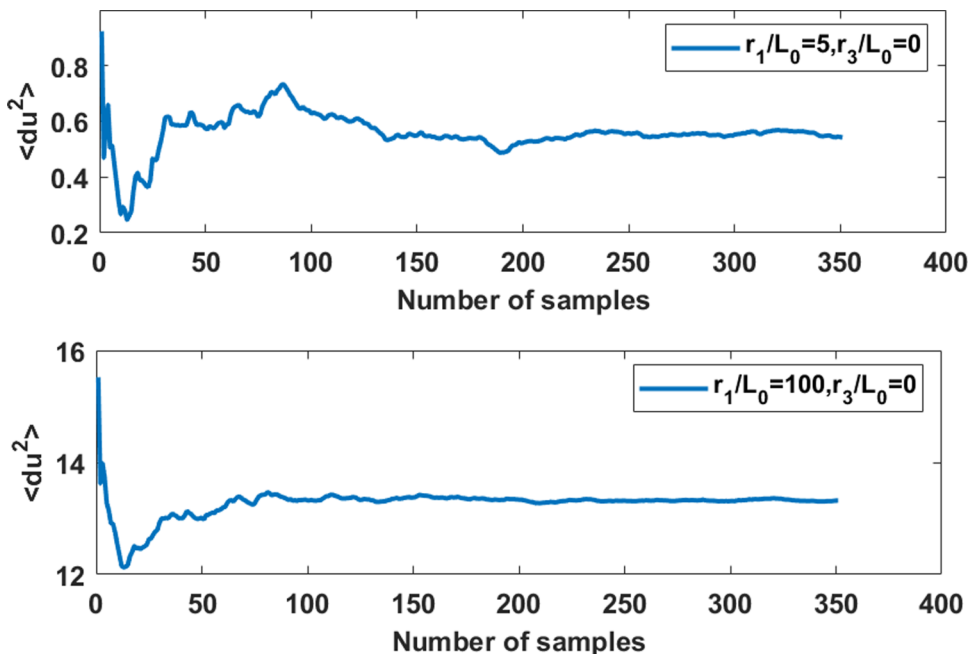


FIG. 18. Running average of $\langle du^2 \rangle$ versus the number of samples at a streamwise location inside the fully turbulent region, $(X - X_0)/L_0 = 2415$, at the fixed height $Y/L_0 = 1.3$ and two different r_1 separations.

distance is fixed at $Y/L_0 = 1.3$. The top panel represents a small streamwise separation, $r_1/L_0 = 5$, and the bottom panel a larger separation, $r_1/L_0 = 100$.

-
- [1] M. V. Morkovin, On the many faces of transition, in *Viscous Drag Reduction* (Springer, Berlin, 1969), pp. 1–31.
 - [2] P. Klebanoff, Effect of free-stream turbulence on a laminar boundary layer, *Bull. Am. Phys. Soc.* **10**, 1323 (1971).
 - [3] K. J. A. Westin, A. V. Boiko, B. G. B. Klingmann, V. V. Kozlov, and P. H. Alfredsson, Experiments in a boundary layer subjected to free stream turbulence. Part 1. Boundary layer structure and receptivity, *J. Fluid Mech.* **281**, 193218 (1994).
 - [4] M. Matsubara and P. H. Alfredsson, Disturbance growth in boundary layers subjected to free-stream turbulence, *J. Fluid Mech.* **430**, 149 (2001).
 - [5] J. H. Fransson, M. Matsubara, and P. H. Alfredsson, Transition induced by free-stream turbulence, *J. Fluid Mech.* **527**, 1 (2005).
 - [6] R. Jacobs and P. Durbin, Simulations of bypass transition, *J. Fluid Mech.* **428**, 185 (2001).
 - [7] L. Brandt, P. Schlatter, and D. S. Henningson, Transition in boundary layers subject to free-stream turbulence, *J. Fluid Mech.* **517**, 167 (2004).
 - [8] T. A. Zaki and P. A. Durbin, Mode interaction and the bypass route to transition, *J. Fluid Mech.* **531**, 85 (2005).
 - [9] V. Ovchinnikov, M. M. Choudhari, and U. Piomelli, Numerical simulations of boundary-layer bypass transition due to high-amplitude free-stream turbulence, *J. Fluid Mech.* **613**, 135 (2008).
 - [10] J. Hunt and P. Durbin, Perturbed vortical layers and shear sheltering, *Fluid Dynam. Res.* **24**, 375 (1999).
 - [11] T. A. Zaki and S. Saha, On shear sheltering and the structure of vortical modes in single-and two-fluid boundary layers, *J. Fluid Mech.* **626**, 111 (2009).
 - [12] J. M. Kendall, Studies on laminar boundary-layer receptivity to freestream turbulence near a leading edge, in *Boundary Layer Stability and Transition to Turbulence. Proceedings of the Symposium, ASME and JSME Joint Fluids Engineering Conference, 1st, Portland, OR, June 23–27, 1991* (American Society of Mechanical Engineers, New York, 1991), pp. 23–30.
 - [13] O. M. Phillips, Shear-flow turbulence, *Annu. Rev. Fluid Mech.* **1**, 245 (1969).
 - [14] L. Brandt, The lift-up effect: the linear mechanism behind transition and turbulence in shear flows, *Eur. J. Mech. B/Fluids* **47**, 80 (2014).
 - [15] M. Landahl, A note on an algebraic instability of inviscid parallel shear flows, *J. Fluid Mech.* **98**, 243 (1980).
 - [16] P. A. Durbin, Perspectives on the phenomenology and modeling of boundary layer transition, *Flow Turbul. Combust.* **99**, 1 (2017).
 - [17] P. Schlatter, L. Brandt, H. De Lange, and D. S. Henningson, On streak breakdown in bypass transition, *Phys. Fluids* **20**, 101505 (2008).
 - [18] N. J. Vaughan and T. A. Zaki, Stability of zero-pressure-gradient boundary layer distorted by unsteady klebanoff streaks, *J. Fluid Mech.* **681**, 116 (2011).
 - [19] M. Hack and T. Zaki, Streak instabilities in boundary layers beneath free-stream turbulence, *J. Fluid Mech.* **741**, 280 (2014).
 - [20] H. Emmons, The laminar-turbulent transition in a boundary layer. Part I, *J. Aeronaut. Sci.* **18**, 490 (1951).
 - [21] I. Wygnanski, M. Sokolov, and D. Friedman, On a turbulent spot in a laminar boundary layer, *J. Fluid Mech.* **78**, 785 (1976).
 - [22] A. Perry, T. Lim, and E. Teh, A visual study of turbulent spots, *J. Fluid Mech.* **104**, 387 (1981).
 - [23] E. C. Itsweire and C. W. Van Atta, An experimental investigation of coherent substructures associated with turbulent spots in a laminar boundary layer, *J. Fluid Mech.* **148**, 319 (1984).
 - [24] R. J. Anthony, T. V. Jones, and J. E. LaGraff, High frequency surface heat flux imaging of bypass transition, in *ASME Turbo Expo 2004: Power for Land, Sea, and Air* (American Society of Mechanical Engineers, New York, 2004), pp. 185–195.

- [25] X. Wu, P. Moin, J. M. Wallace, J. Skarda, A. Lozano-Durán, and J.-P. Hickey, Transitional–turbulent spots and turbulent–turbulent spots in boundary layers, *Proc. Natl. Acad. Sci. USA* **114**, E5292 (2017).
- [26] K. P. Nolan and T. A. Zaki, Conditional sampling of transitional boundary layers in pressure gradients, *J. Fluid Mech.* **728**, 306 (2013).
- [27] O. Marxen and T. A. Zaki, Turbulence in intermittent transitional boundary layers and in turbulence spots, *J. Fluid Mech.* **860**, 350 (2019).
- [28] B. Eckhardt, K. Marzinzik, and A. Schmiegell, Transition to turbulence in shear flows, in *A Perspective Look at Nonlinear Media* (Springer, Berlin, 1998), pp. 327–338.
- [29] J. H. M. Fransson and P. H. Alfredsson, On the disturbance growth in an asymptotic suction boundary layer, *J. Fluid Mech.* **482**, 5190 (2003).
- [30] P. Andersson, M. Berggren, and D. S. Henningson, Optimal disturbances and bypass transition in boundary layers, *Phys. Fluids* **11**, 134 (1999).
- [31] P. Luchini, Reynolds-number-independent instability of the boundary layer over a flat surface: Optimal perturbations, *J. Fluid Mech.* **404**, 289309 (2000).
- [32] P. A. Davidson, *Turbulence: An Introduction for Scientists and Engineers* (Oxford University Press, New York, 2015).
- [33] R. J. Hill, Equations relating structure functions of all orders, *J. Fluid Mech.* **434**, 379 (2001).
- [34] R. J. Hill, Exact second-order structure-function relationships, *J. Fluid Mech.* **468**, 317 (2002).
- [35] N. Marati, C. Casciola, and R. Piva, Energy cascade and spatial fluxes in wall turbulence, *J. Fluid Mech.* **521**, 191 (2004).
- [36] F. Alves Portela, G. Papadakis, and J. Vassilicos, The turbulence cascade in the near wake of a square prism, *J. Fluid Mech.* **825**, 315 (2017).
- [37] R. Gomes-Fernandes, B. Ganapathisubramani, and J. Vassilicos, The energy cascade in near-field non-homogeneous non-isotropic turbulence, *J. Fluid Mech.* **771**, 676 (2015).
- [38] S. B. Pope, *Turbulent Flows* (Cambridge University Press, Cambridge, UK, 2001).
- [39] I. Paul, G. Papadakis, and J. C. Vassilicos, Genesis and evolution of velocity gradients in near-field spatially developing turbulence, *J. Fluid Mech.* **815**, 295332 (2017).
- [40] D. Xiao and G. Papadakis, Nonlinear optimal control of bypass transition in a boundary layer flow, *Phys. Fluids* **29**, 054103 (2017).
- [41] D. Xiao and G. Papadakis, Nonlinear optimal control of transition due to a pair of vortical perturbations using a receding horizon approach, *J. Fluid Mech.* **861**, 524555 (2019).
- [42] P. Roach, The influence of a turbulent free-stream on zero pressure gradient transitional boundary layer development: Part 1. Test cases T3A and T3B, in *Numerical Simulation of Unsteady Flows and Transition to Turbulence: Proceedings of the ERCOFTAC Workshop Held at EPFL, 26–28 March 1990, Lausanne, Switzerland* (Cambridge University Press, Cambridge, UK, 1990).
- [43] G. Taylor, *Some Recent Developments in the Study of Turbulence* (Wiley, New York, 1939).
- [44] N. Otsu, A threshold selection method from gray-level histograms, *IEEE Trans. Syst. Man Cybernet.* **9**, 62 (1979).
- [45] R. Narasimha, The laminar-turbulent transition zone in the boundary layer, *Prog. Aerospace Sci.* **22**, 29 (1985).
- [46] P. A. Davidson, T. B. Nickels, and P.-Å. Krogstad, The logarithmic structure function law in wall-layer turbulence, *J. Fluid Mech.* **550**, 5160 (2006).
- [47] N. Saikrishnan, E. De Angelis, E. K. Longmire, I. Marusic, C. M. Casciola, and R. Piva, Reynolds number effects on scale energy balance in wall turbulence, *Phys. Fluids* **24**, 015101 (2012).